



Physical Characterization of Interstellar Comet 2I/2019 Q4 (Borisov)

Man-To Hui (許文韜)¹, Quan-Zhi Ye (葉泉志)², Dora Föhning¹, Denise Hung¹, and David J. Tholen¹

¹Institute for Astronomy, University of Hawai'i, 2680 Woodlawn Drive, Honolulu, HI 96822, USA; manto@ifa.hawaii.edu

²Department of Astronomy, University of Maryland, College Park, MD 20742, USA

Received 2020 March 30; revised 2020 June 10; accepted 2020 June 16; published 2020 July 31

Abstract

We present a study of interstellar comet 2I/2019 Q4 (Borisov) using both preperihelion and postperihelion observations spanning late September 2019 through late January 2020. The intrinsic brightness of the comet was observed to continuously decline throughout the timespan, likely due to the decreasing effective scattering cross-section as a result of volatile sublimation with a slope of $-0.43 \pm 0.02 \text{ km}^2 \text{ d}^{-1}$. We witnessed no significant change in the slightly reddish color of the comet, with mean values of $\langle g - r \rangle = 0.68 \pm 0.04$, $\langle r - i \rangle = 0.23 \pm 0.03$, and the normalized reflectivity gradient across the g and i bands $\overline{S'}(g, i) = (10.6 \pm 1.4)\%$ per 10^3 \AA , all unremarkable in the context of solar system comets. Using the available astrometric observations, we confidently detect the nongravitational acceleration of the comet following a shallow heliocentric distance dependence of $r_H^{-1 \pm 1}$. Accordingly, we estimate that the nucleus is most likely $\lesssim 0.4 \text{ km}$ in radius, and that a fraction of $\gtrsim 0.2\%$ of the total mass of the nucleus has been eroded due to the sublimation activity since the earliest observation of the comet in 2018 December by the time of perihelion. Our morphology simulation suggests that the dust ejection speed increased from $\sim 4 \text{ m s}^{-1}$ in 2019 September to $\sim 7 \text{ m s}^{-1}$ around perihelion for the optically dominant dust grains with $\beta \sim 0.01$, and that the observable dust grains are no smaller than micron size.

Unified Astronomy Thesaurus concepts: Comets (280)

1. Introduction

Cometary object 2I/2019 Q4 (Borisov) (formerly C/2019 Q4, hereafter “2I”) was discovered by G. Borisov on 2019 August 30 at apparent R -band magnitude $m_R \approx 18$ with a $\sim 7''$ condensed coma.³ The orbital eccentricity of 2I is significantly hyperbolic ($e = 3.36$), indicating that 2I is not bound to the solar system and has an interstellar origin (Higuchi & Kokubo 2019). Thus, 2I is the second interstellar small body ever observed in the solar system after 1I/2017 U1 (‘Oumuamua) (Dybczyński & Królikowska 2018). As opposed to ‘Oumuamua, which appeared completely asteroidal in optical images by various observers (e.g., Bannister et al. 2017; Jewitt et al. 2017; Knight et al. 2017), 2I has been exhibiting an obvious cometary feature, indistinguishable from ordinary comets in the solar system in terms of its morphology and color from the earliest observations since the discovery (Fitzsimmons et al. 2019; Guzik et al. 2019; Jewitt & Luu 2019; Opitom et al. 2019). Therefore 2I is observationally the first known interstellar comet that visits the solar system. Remarkably, Ye et al. (2020) successfully identified 2I in pre-discovery data from the Zwicky Transient Facility (ZTF) all the way back to mid-December 2018, when the object was $\sim 8 \text{ au}$ from the Sun. Furthermore, 2I appears to be chemically distinct from the majority of the known solar system comets, because the interstellar interloper was observed to contain substantially more carbon monoxide (CO) than water (H_2O) gas than any previously measured comets in the inner solar system (Bodewits et al. 2020; Cordiner et al. 2020), possibly indicating that the chemical composition of the protoplanetary disk where 2I is appreciably different from our own.

In order to understand how 2I would evolve as it approached the Sun and constraints on the physical characteristics of the

object in contrast to typical solar system comets, we monitored 2I from late September 2019 to late January 2020, covering an arc from over two months prior to the perihelion passage ($t_p = \text{TDB } 2019 \text{ December } 8.6$) to almost two months postperihelion. The paper is structured in the following manner. We describe the observations in Section 2, give results and analyses in Section 3, present discussions in Section 4, and conclude in Section 5.

2. Observations

We conducted observations of 2I using the University of Hawaii (UH) 2.2 m telescope and a Tektronix 2048 \times 2048 CCD camera at the $f/10$ Cassegrain focus, through g' -, r' -, and I -band filters. To improve the temporal coverage of the comet, we included in our analysis publicly available data from the 0.6 m NEXT telescope at Xingming Observatory located in Xinjiang, China. Images from the UH 2.2 m telescope were tracked considerably following the apparent motion of the comet. Due to a mechanical failure of the camera’s filter wheel in December 2019 and the fact that the primary observations on these nights were made in white light, only unfiltered images of the comet were taken on 2019 December 24 and 2020 January 1. The images have a square field of view (FOV) of $7'.5 \times 7'.5$, and were 2×2 binned on chip, resulting in an image scale of $0''.44 \text{ pixel}^{-1}$. In order to mitigate artefacts such as cosmic-ray hits, bad CCD columns, and dead pixels, we dithered images between exposures. Seeing during these observations varied between $\sim 0''.7$ and $1''.0$, typically $\sim 0''.8$ (FWHM of field stars).

We also included data acquired from NEXT to improve the temporal coverage of the comet. The images were initially taken through $BVRI$ filters, and were later switched to the Sloan gri system from early October 2019 after a renovation of the observatory. Since the telescope could only follow the comet at a sidereal rate, an individual exposure time of 120 s was set so as to keep the trailing of the comet visually unnoticeable. The

³ See Minor Planet Electronic Circular 2019-R106 (<https://minorplanetcenter.net/mpec/K19/K19RA6.html>).

images have an image scale of $0''.63 \text{ pixel}^{-1}$ in the 1×1 binning mode, with a FOV of $21''.5 \times 21''.5$. Seeing at NEXT, typically $\sim 2''\text{--}3''$, was incomparable to that at the UH 2.2 m telescope, owing to a much lower elevation of the observatory.

All of the images were calibrated in a standard fashion, i.e., bias frames taken from each night were subtracted, and the images were divided by flat-field frames that were generated from the science images in the same filters from the same nights, or neighboring nights in a few cases, to fully eradicate influences from field stars and the comet. An additional step for the NEXT data was that dark frames were subtracted from the images before flatfielding. Cosmic rays and bad pixels were removed by L.A. Cosmic (van Dokkum 2001) and the IRAF task `cosmicrays`.

We show the observing geometry of 2I in Figure 1, and coadded images of the comet from the UH 2.2 m telescope and NEXT in Figures 2 and 3, respectively.

3. Analysis

3.1. Photometry

Photometric measurements were performed slightly differently on images from the two telescopes. For data taken from the UH 2.2 m telescope, we measured the flux of 2I in the individual images, whereas for data from NEXT, we measured the flux on nightly median combined images through the same filters with alignment on the apparent motion of the comet. The aperture has a fixed projected linear radius of $\varrho = 10^4 \text{ km}$ at the topocentric distance of the comet so as to minimize potential biases from the aperture effect. The angular size of the chosen photometric aperture ($\gtrsim 4''.6$ in radius) is always larger than the seeing FWHM while the signal-to-noise ratio (S/N) is close to maximal. The sky background was computed from a concentric annulus with inner and outer radii of $3\times$ and $6\times$ the photometric aperture radius. We have made tests by changing the size of the annulus, but the results are always consistent within uncertainties, which were determined from Poisson statistics of the CCD. We have also repeated the measurements with a fixed aperture of $\varrho = 1.5 \times 10^4 \text{ km}$ in radius. The general shape of the light curve of the comet is the same, but with larger uncertainties and visually slightly greater scatter due to a decrease in the S/N of the comet. So we conclude that our results should be robust.

On a few occasions for the UH 2.2 m observations taken prior to late January 2020, there are faint field stars that partly fall within the photometric aperture in some of the images. To clean the contamination, we first extracted a number of field stars from the same individual images using StarFinder (Diolaiti et al. 2000), then fitted and obtained trailed point-spread function (PSF) models, which were scaled by brightness and subtracted from the images. These stars have all been cleaned nicely, leaving no noticeable artefacts in the photometric aperture. In late January 2020, the comet was near the Galactic equator and therefore the FOVs are packed with stars. We computed nightly median images registered on field stars in respective filters, in which the comet was removed nicely. These median images were used as templates for optimal subtraction with High Order Transform of PSF ANd Template Subtraction (HOTPANTS; Becker 2015), resulting in a much cleaner sky background. For the NEXT images, contamination of faint field stars is not a concern because they were removed in the nightly median combined stacks.

Image zero-points of the UH 2.2 m telescope were obtained from photometry of field stars in the individual images using an aperture of 9 pixels ($\sim 4''.0$) in radius, whereas for the NEXT

data, we measured the image zero-points on nightly median combined stacks with alignment of field stars using an aperture of 10 pixels ($\sim 6''.3$) in radius. Such apertures are large enough to enclose the majority of flux of the field stars and avoid aperture corrections due to varying seeing. Sky backgrounds were measured with a sky annulus having inner and outer radii $1.5\times$ and $2.5\times$ the corresponding aperture radii. Magnitudes of the field stars were taken from the Pan-STARRS1 (PS1) Data Release 1 (DR1; Flewelling et al. 2016), and were transformed from the PS1 system to the corresponding photometric bands using equations in Tonry et al. (2012) for all of the observations but those from 2019 December 26 and thereafter, when the comet was at decl. $< -30^\circ$. In these cases we switched to the AAVSO Photometric All-Sky Survey Data Release 10 (Henden et al. 2018).⁴ As for the unfiltered observations from the UH 2.2 m telescope, we initially included a linear color slope to color index $g - r$. However, after tests we immediately discovered that the color slope is statistically zero at the 1σ level determined from field stars having color indices in the range $0.3 \leq g - r \leq 1.0$, and therefore we ignored the color term in the final version of the photometric reduction.

No significant systematic trend in the light curve of 2I is seen over the timespans (all lasted $< 1 \text{ hr}$) from our observing nights from the UH 2.2 m telescope, likely due to coma dilution (Jewitt 1991). Thus, we only present the weighted mean apparent magnitude of 2I and the corresponding standard deviation of the repeated measurements in the same filters from the same nights in Figure 4(a), together with measurements from NEXT.

The observing geometry of the comet varied considerably during our observation campaign, and thus must be corrected so as to investigate the intrinsic brightness of the comet from its apparent magnitude, denoted as $m_\lambda(r_H, \Delta, \alpha)$, where r_H and Δ are respectively the heliocentric and topocentric distances of the comet, and α is the phase angle, via the following equation:

$$m_\lambda(1, 1, 0) = \underbrace{m_\lambda(r_H, \Delta, \alpha) - 5 \log(r_H \Delta)}_{m_\lambda(1, 1, \alpha)} + 2.5 \log \phi(\alpha). \quad (1)$$

Here, $m_\lambda(1, 1, \alpha)$ is termed the reduced magnitude, and ϕ is the phase function of the comet, which is assumed to resemble those of the solar system comets and is approximated by the empirical Halley–Marcus phase function by Marcus (2007) and Schleicher & Bair (2011) (see Section 4.1 for further discussions of the phase-angle correction). We present the results in Figure 4(b). We thus notice that, although the apparent brightness of 2I was increasing on its way to perihelion and started to fade afterwards, the intrinsic brightness in fact has been steadily decreasing since our earliest observation of the comet from the UH 2.2 m telescope in 2019 September. This result appears to contradict the earliest observations of the comet that cover much shorter timespans (Jewitt & Luu 2019; Jewitt et al. 2020).

3.2. Nongravitational Acceleration

We obtained astrometry of 2I in the r -band images and the unfiltered ones from the nights when the filter wheel malfunctioned at the UH 2.2 m telescope with reduction using

⁴ Accessible at <https://www.aavso.org/apass-dr10-download>.

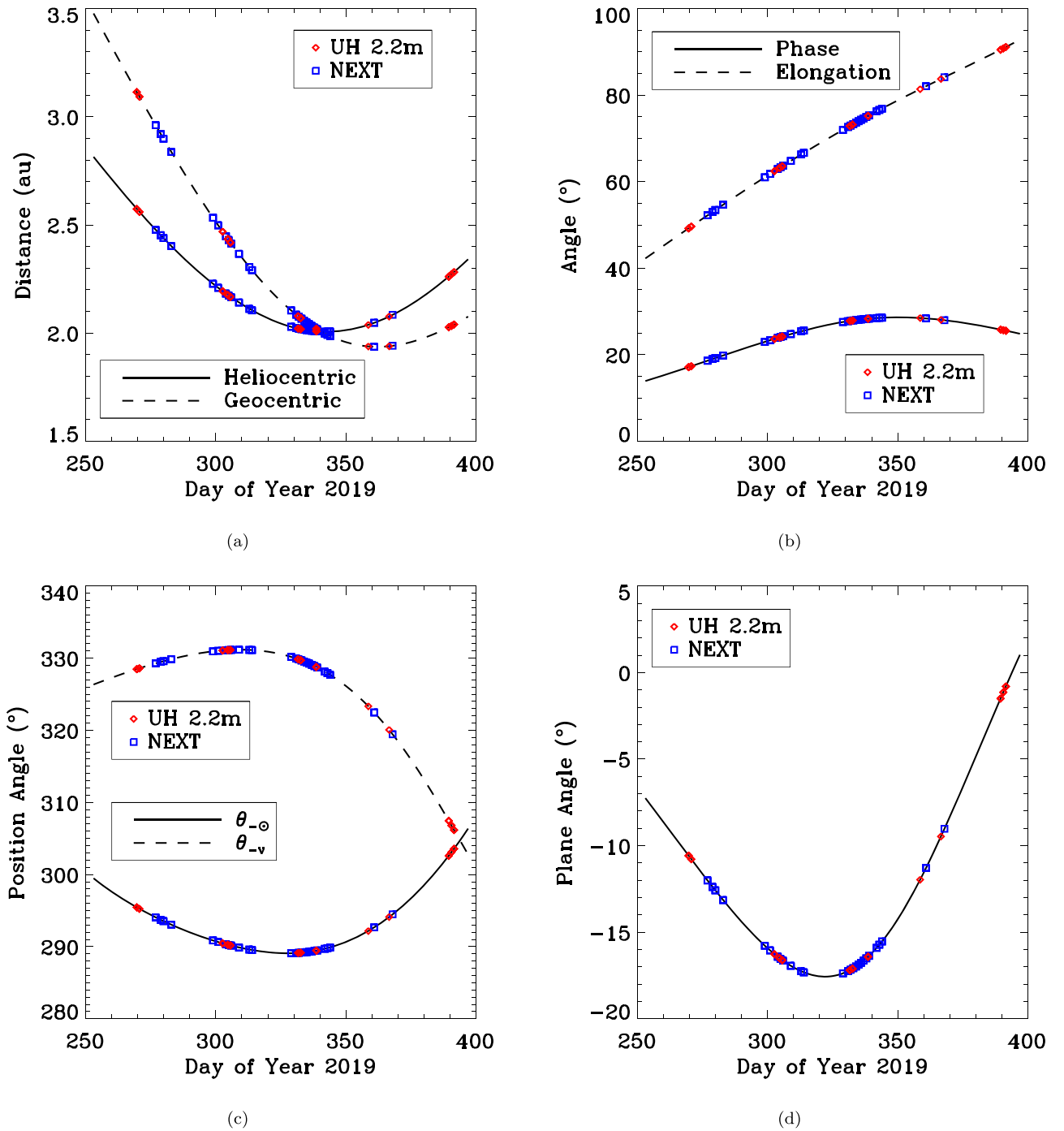


Figure 1. Observing geometry of interstellar comet 2I/2019 Q4 (Borisov) in terms of (a) heliocentric and geocentric distances, (b) phase angle and solar elongation, (c) position angles of projected antisolar direction ($\theta_{-\odot}$) and negative heliocentric velocity (θ_{-v}), and (d) the plane angle of the comet as a function of time during our observing campaign from the UH 2.2 m telescope (red diamonds) and NEXT (blue squares).

the Gaia DR2 catalog (Gaia Collaboration et al. 2018). No astrometric measurement was done with the NEXT images because of the low S/N of the comet and much worse seeing. Astrometric observations from other stations, downloaded from the Minor Planet Center (MPC) Observation Database,⁵ in combination with our measurements, were then fed into orbit determination code FindOrb.⁶ We debiased the astrometry by following the method described in Farnocchia et al. (2015),

⁵ https://minorplanetcenter.net/db_search

⁶ https://www.projectpluto.com/find_orb.htm

followed by assignment of a weighting scheme detailed in Vereš et al. (2017) for observations downloaded from the MPC. This procedure was used because many observations are reported without positional uncertainties, and in cases for which they were reported, the MPC is not yet exporting them. Our astrometric measurements and those from the ZTF, including the pre-discovery observations by Ye et al. (2020), were weighted by the measured positional uncertainties. In addition to the gravitational force exerted by the Sun, perturbations from the eight major planets, Pluto, the Moon, and the most massive 16 main-belt asteroids, and the relativistic

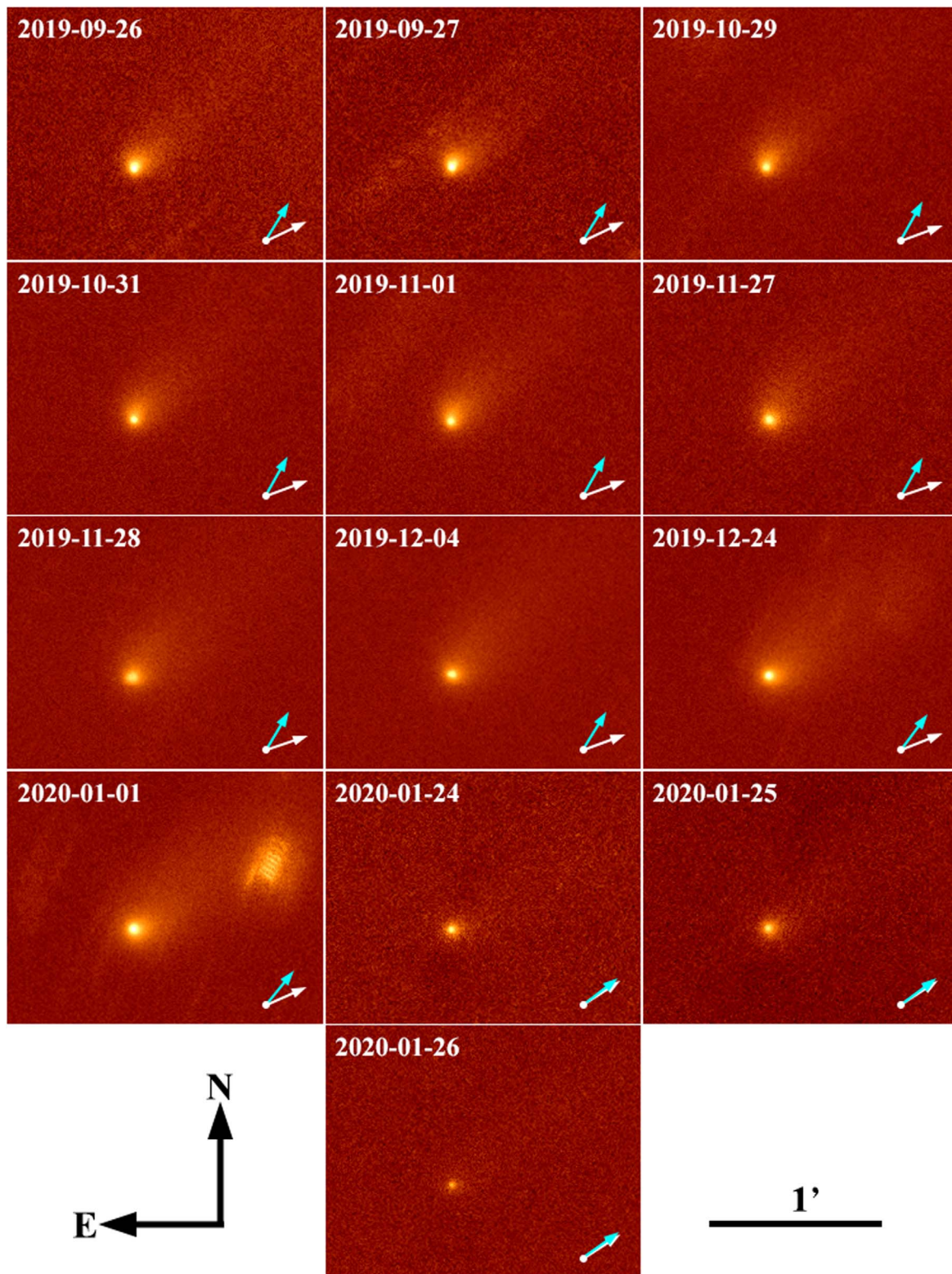


Figure 2. Median coadded images from the UH 2.2 m telescope of interstellar comet 2I/2019 Q4 (Borisov). The two images from 2019 December 24 and 2020 January 1 are unfiltered due to the filter wheel issue, but the others are in the r band. The trails in some of the panels are uncleaned artefacts from bright background stars. As indicated by the compass in the lower left, equatorial north is up and east is left. A scale bar of $1'$ in length is shown. Also labeled are the position angles of the antisolar direction (white arrow) and the negative heliocentric velocity projected onto the sky plane (cyan arrow). Note that in late January 2020, as Earth was to cross the orbital plane of the comet, the two arrows increasingly overlap.

corrections were taken into account, although these were found to be unimportant in comparison to the gravitational effect from the Sun. The planetary and lunar ephemerides DE 431 (Folkner et al. 2014) were utilized.

Initially we attempted to determine a gravity-only orbit solution to the astrometric observations of 2I. However, we soon found that there exists a strong systematic trend in the astrometric residuals that could not be removed no matter how

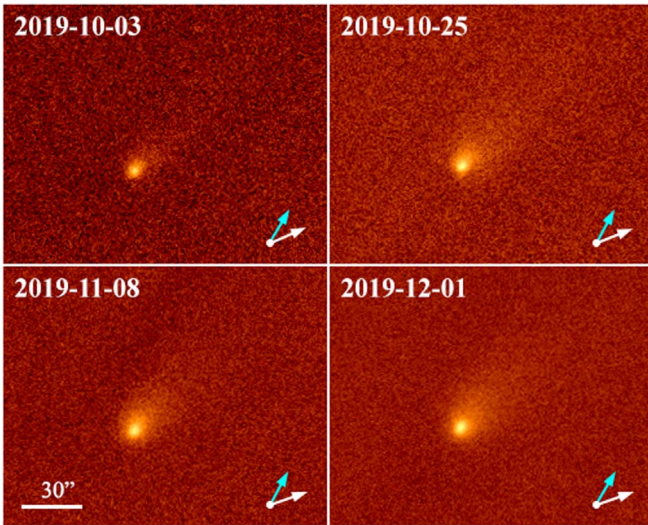


Figure 3. Selected examples of median coadded images from the 0.6 m NEXTE telescope of interstellar comet 2I/2019 Q4 (Borisov). Only the image from 2019 October 3 is in the R band; the rest are in the r band after a renovation at Xingming Observatory. All images have the equatorial north up and east left. A scale bar of $30''$ in length is shown. As in Figure 2, the position angles of the antisolar direction (white arrow) and the negative heliocentric velocity projected onto the sky plane (cyan arrow) are labeled.

we adjusted the residual cutoff threshold. For example, the majority of our astrometric measurements from late January 2020 would have astrometric residuals $\gtrsim 5\sigma$, with one even exhibiting a deviation at $\sim 11\sigma$, whereas the ZTF prediscovery positions deviate from the calculated positions by $\gtrsim 5\sigma$. The systematic trend remains even if we opt to discard the ZTF prediscovery observations. Therefore, we decided to further include the radial, transverse, and normal (RTN) nongravitational parameters, corresponding to A_j ($j = 1, 2, 3$), which were first introduced by Marsden et al. (1973) and have now been widely applied, as free parameters to be solved in FindOrb. Instead of directly adopting the nongravitational force model of Marsden et al. (1973) based on isothermal sublimation of water ice, for reasons described in Hui & Jewitt (2017), we tested models scaled as r_H^{-n} and varied the power-law index n . Astrometry data with residuals in excess of $3''$ were rejected as outliers.⁷

The obtained results, including those from the model of Marsden et al. (1973) to form a comparison, are presented in Table 1. We clearly see that the nongravitational force models with heliocentric distance dependences of $\sim r_H^{-1\pm 1}$ provide the best fits among the models we tested. Importantly, the strong systematic trend in the astrometric residuals no longer exists in the best fits. In particular, the astrometric residuals of our measurements and those from the ZTF are always at the $\lesssim 1\sigma$ level. Had a steep heliocentric distance dependence for the nongravitational force model been more suitable, the magnitude of the out-of-plane nongravitational parameter A_3 would be unusually enormous in the context of small bodies in the solar system (referenced to the JPL Small-Body Database Search Engine). We thereby infer that it is most unlikely that the mass-loss rate of 2I varies steeply with the heliocentric distance. In this regard, 2I is distinct from comet 67P/

Churyumov–Gerasimenko, the target of the Rosetta mission, with a steeper heliocentric distance dependence for the mass-loss rate (e.g., $\sim r_H^{-5.6}$ for H_2O ; Fougere et al. 2016; Combi et al. 2020), and thereby a significantly steeper power-law nongravitational acceleration preferred by the fit to all of its astrometric data since 1995 (steeper than $\sim r_H^{-4}$; D. Farnocchia 2020, private communication).

We note that the fit with the isothermal H_2O -ice sublimation model of Marsden et al. (1973) is worse than any of the models with $\sim r_H^{-n}$ for $-1 \leq n \leq 5$ (Table 1). Although the astrometric residuals of the ZTF prediscovery observations are considerably smaller than those in the gravity-only solution, they are still $\gtrsim 2''$ and only half of them are at the $\lesssim 1\sigma$ level. The poor fit strongly indicates that the nucleus of 2I is not subject to a nongravitational acceleration following the model of Marsden et al. (1973), in which they assumed isothermal sublimation activity of water ice without a mantle layer. This finding might also call into question the applicability of the model of Marsden et al. (1973) to general solar system comets.

4. Discussion

4.1. Phase Function

When calculating the intrinsic brightness of 2I, we realized the actual phase function of the comet has a predominant influence on the result, because the phase angle varied nontrivially during the time period of our observing campaign. Thus, we feel the importance and necessity to discuss the phase function of 2I here.

In Figure 5, we plot the reduced r -band magnitude of 2I (denoted as $m_r(1, 1, \alpha)$, see its definition in Equation (1)) versus the phase angle, from which we can see that the data points from our earliest observations of the comet to those at maximum phase angle $\alpha \approx 30^\circ$ (roughly corresponding to preperihelion epochs) appear to vary linearly with the phase angle. However, the trend for the data points starting from mid-December 2019, when the phase angle began to decrease, is totally in disagreement with the earlier trend, indicating a change in the postperihelion activity of the comet. The obtained best-fit linear phase coefficient using the data points of the r -band magnitude from the whole timespan and the goodness of the fit are given in Table 2, where we can see that the reduced chi-squared value is $\gg 1$, suggesting an exceptionally poor fit. If we only fit the preperihelion part, however, the goodness of the fit is much improved. Nevertheless, the best-fit phase coefficient, $\beta_\alpha = 0.0505 \pm 0.0010 \text{ mag deg}^{-1}$, is larger than that for many (if not all) of the known solar system comets ($0.02 \lesssim \beta_\alpha \lesssim 0.04 \text{ mag deg}^{-1}$; Meech & Jewitt 1987; Bertini et al. 2019). We note that a considerably steeper backscattering phase function of the near-nucleus coma of comet 67P/Churyumov–Gerasimenko at small phase angles was reported from the Rosetta mission by Fink & Doose (2018), who attribute the phenomenon to the presence of large transparent particles (at least micron size, and the imaginary index of refraction $\lesssim 10^{-2}$) from the nucleus in the region. Using the best-fit parameters and including the measurement uncertainties of Fink & Doose (2018), we obtained that the 3σ upper limit to the phase coefficient in the same range of phase angle as the one during our observed time period of 2I is $\beta_\alpha = 0.042 \text{ mag deg}^{-1}$, which is inconsistent with the best-fit phase coefficient value we found for 2I (Table 2) at the 3σ level. By no means can we completely rule out the possibility that 2I

⁷ We have tested that even if we skip the step of outlier rejection, the resulting RTN nongravitational parameters are statistically similar to the ones with the step performed within the 1σ level.

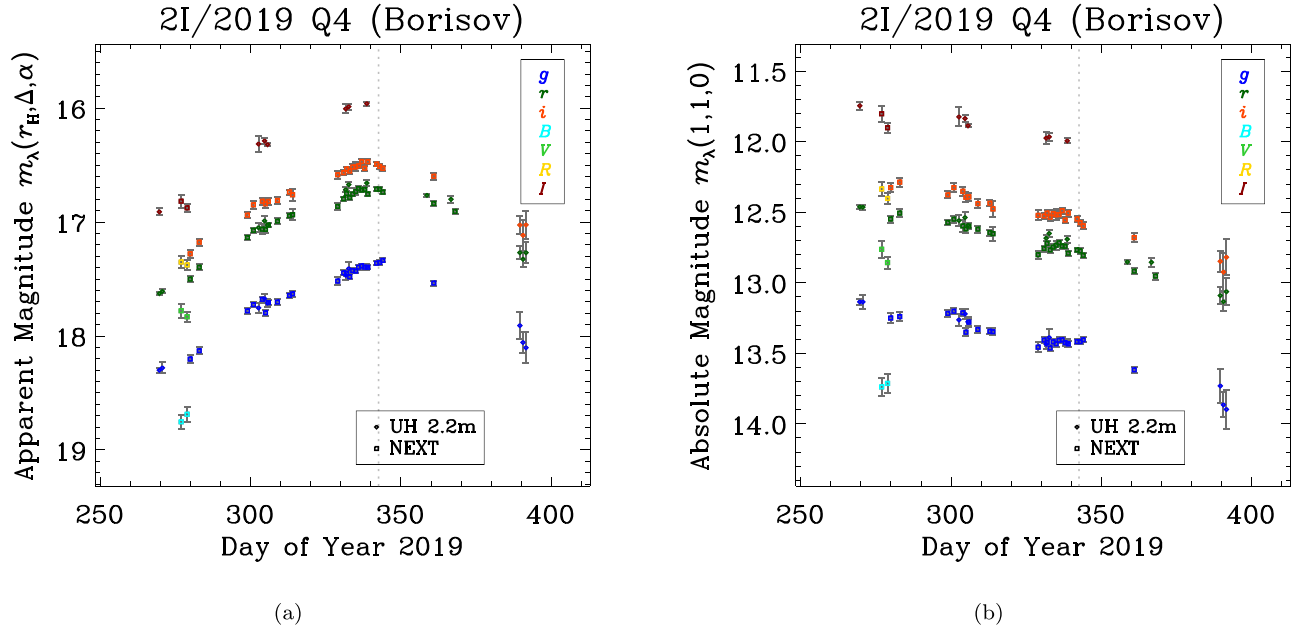


Figure 4. The apparent (a) and intrinsic (b) light curves of interstellar comet 2I/2019 Q4 (Borisov) as functions of time during our observing campaign from the UH 2.2 m telescope (diamonds) and NEXT (squares). The reduction bands are color coded as indicated in the legend. Panel (b) was obtained by applying Equation (1) to normalize the apparent magnitude of the comet in panel (a) to $r_H = \Delta = 1$ au and $\alpha = 0^\circ$. Assuming that 2I has a phase function similar to those of solar system comets, and thereby approximated by the empirical Halley–Marcus function by Marcus (2007) and Schleicher & Bair (2011), we can note in panel (b) that its intrinsic brightness has been fading since our earliest observation from late September 2019. The vertical gray dotted line in each of the panels marks the perihelion epoch of the comet ($t_p =$ TDB 2019 December 8.6).

Table 1
Nongravitational Parameters of Comet 2I/2019 Q4 (Borisov)

Nongravitational Force Model	Nongravitational Parameters (au d ⁻²)			Mean Residuals (arcsec)
	Radial A_1	Transverse A_2	Normal A_3	
$\sim r_H^{-n}$ Power-law Index $n = -1$	$(+2.54 \pm 0.14) \times 10^{-9}$	$(-1.27 \pm 2.17) \times 10^{-10}$	$(-6.00 \pm 1.08) \times 10^{-10}$	± 0.88830
0	$(+4.52 \pm 0.41) \times 10^{-9}$	$(-1.69 \pm 5.66) \times 10^{-10}$	$(-2.09 \pm 0.39) \times 10^{-9}$	± 0.88790
+1	$(+7.12 \pm 1.08) \times 10^{-9}$	$(-1.33 \pm 1.26) \times 10^{-9}$	$(-6.66 \pm 1.03) \times 10^{-9}$	± 0.88781
+2	$(+1.19 \pm 0.24) \times 10^{-8}$	$(-2.78 \pm 2.49) \times 10^{-9}$	$(-1.63 \pm 0.22) \times 10^{-8}$	± 0.88796
+3	$(+2.26 \pm 0.49) \times 10^{-8}$	$(-3.28 \pm 4.86) \times 10^{-9}$	$(-3.53 \pm 0.44) \times 10^{-8}$	± 0.88832
+4	$(+4.55 \pm 0.99) \times 10^{-8}$	$(+1.08 \pm 9.69) \times 10^{-9}$	$(-7.35 \pm 0.88) \times 10^{-8}$	± 0.88874
+5	$(+9.33 \pm 2.00) \times 10^{-8}$	$(+8.37 \pm 19.66) \times 10^{-9}$	$(-1.51 \pm 0.18) \times 10^{-7}$	± 0.88914
H ₂ O-ice sublimation ^a	$(+2.80 \pm 0.58) \times 10^{-8}$	$(+7.39 \pm 5.83) \times 10^{-9}$	$(-4.51 \pm 0.51) \times 10^{-8}$	± 0.88998

Notes. Uncertainties of the nongravitational parameters are formal 1σ errors. We included the same 2842 out of a total of 2994 astrometric observations from 2018 December 13 to 2020 February 27 to obtain the solutions for all of the models. Observations with residuals in excess of $3''$ were regarded as outliers. See Section 3.2 for detailed information.

^a The isothermal model of Marsden et al. (1973).

has a phase function steeper than any of the known solar system comets. This scenario would require that the preperihelion activity of the comet would remain nearly constant, followed by a decline in its postperihelion activity. However, given the similarities between 2I and solar system comets, we prefer that the decline in the intrinsic brightness of 2I shown in Figure 4(b) is due to the change in its activity.

4.2. Color

We plot the color indices $g - r$ and $r - i$ of comet 2I versus both time and the heliocentric distance in Figure 6. The transformation by Jordi et al. (2006) was applied to transform the color of the comet in the Johnson–Cousin system to the Sloan Digital Sky Survey system. Generally speaking, similar to solar

system comets, the color of 2I was slightly redder than the color of the Sun ($(g - r)_\odot = +0.46 \pm 0.02$, $(r - i)_\odot = +0.12 \pm 0.02$; Willmer 2018) during our observing campaign from the UH 2.2 m telescope and NEXT. Given the uncertainties, we cannot confidently spot any change in the color of the comet, and thus derive the mean values of the color indices as $\langle g - r \rangle = +0.68 \pm 0.04$ and $\langle r - i \rangle = +0.23 \pm 0.03$. The uncertainties are weighted standard deviations of the data points. Overall, the mean color we found for the comet is consistent with the measurements by other observers (e.g., Bolin et al. 2020; Guzik et al. 2019; Jewitt & Luu 2019; Opitom et al. 2019) if transformed to the same photometric system when necessary.

For completeness we also calculate the normalized reflectivity gradient (A’Hearn et al. 1984; Jewitt & Meech 1986) across

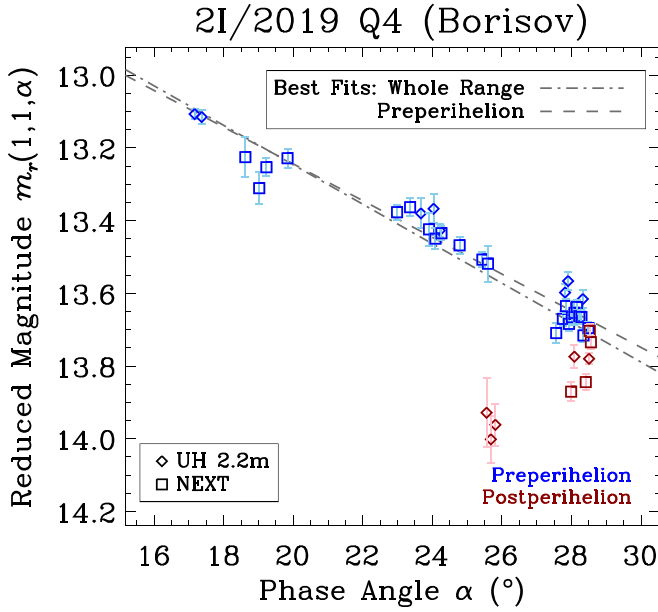


Figure 5. The reduced r -band magnitude of interstellar comet 2I/2019 Q4 (Borisov), $m_r(1, 1, \alpha)$, vs. the phase angle α . Data points from the two observatories are plotted as different symbols, as indicated in the legend in the lower left corner of the figure. Preperihelion and postperihelion data points are in blue and dark red, respectively. The gray dashed–dotted line is the best linear least-squares fit to all of the r -band data, and the less steep dashed line is the best fit to the preperihelion counterparts (see Table 2).

Table 2
Best-fit Phase Coefficients of Interstellar Comet 2I/2019 Q4 (Borisov)

Fitted Range	Phase Coefficient β_α (mag deg $^{-1}$)	Reduced Chi-Squared ^a χ^2_ν
Whole	0.0543 ± 0.0009	9.39
Preperihelion	0.0505 ± 0.0010	2.47

Notes. Only the r -band data points were used to compute the best linear least-squares fits. See Figure 5 for the plot showing comparison between the best fits and the data.

^a Chi-squared per degree of freedom, dimensionless.

the g and i bands of the comet through the following equation:

$$S'(g, i) = \left(\frac{2}{\lambda_i - \lambda_g} \right) \frac{10^{0.4[(g-i)-(g-i)_{(\odot)}]} - 1}{10^{0.4[(g-i)-(g-i)_{(\odot)}]} + 1}, \quad (2)$$

where λ_g and λ_i are the effective wavelengths of the g and i bands, respectively. A negative value of the normalized reflectivity gradient indicates that the color of the object over the filter pair region is bluer than that of the Sun. Otherwise it is redder. We plot the results versus time and the heliocentric distance in Figure 7. The uncertainties are propagated from the errors in the photometric measurements. Again, given the uncertainties of the data points we cannot identify any changes in the normalized reflectivity gradient of the comet. We obtain the mean value as $\overline{S'}(g, i) = (10.6 \pm 1.4)\%$ per 10^3 \AA , which is in agreement with de León et al. (2019), and is by no means outstanding in the context of known solar system comets and asteroids in cometary orbits (e.g., Licandro et al. 2018). However, we are aware that differences in chemical composition between 2I and typical solar system comets have been noticed in

various observations (Bannister et al. 2020; Bodewits et al. 2020; Cordiner et al. 2020; Kareta et al. 2020), the most marked of which is the unusually high CO abundance of 2I. The reason why we see no peculiarity in the broadband color of the comet is likely that the signal we received was dominantly from scattering of sunlight by dust in the coma, rather than from gas emission.

4.3. Morphology

In the morphology of the dust tail of 2I lies the key to physical properties of the cometary dust grains therein. Their trajectories are determined by the initial ejection velocity v_{ej} , the release epoch, and the β parameter, which is the ratio between the solar radiation pressure force and the gravitational force of the Sun, and is related to physical properties of dust grains by

$$\beta = \frac{C_{pr} Q_{pr}}{\rho_d a}. \quad (3)$$

Here, $C_{pr} = 5.95 \times 10^{-4} \text{ kg m}^{-2}$ is the solar radiation pressure coefficient, $Q_{pr} \approx 1$ is the scattering efficiency, a and ρ_d are respectively the radius and the bulk density of the dust grains, assumed to be spherical. As the bulk density of dust grains in the coma of 2I remains unconstrained, we simply assume a constant value of $\rho_d = 0.5 \text{ g cm}^{-3}$, similar to the bulk density of typical solar system cometary nuclei (e.g., Pätzold et al. 2016). The syndyne–synchrone computation (e.g., Finson & Probst 1968) by Jewitt et al. (2020) suggests that the observed optically dominant dust grains of 2I have $\beta \sim 0.01$, equivalent to a dust radius of $a \sim 0.1 \text{ mm}$ given our assumed value of the dust bulk density. However, a shortcoming of the syndyne–synchrone computation is that it ignores the initial ejection velocity of dust v_{ej} , which is physically unrealistic. A crude estimate of the ejection speed of the optically dominant dust grains can be gleaned by measuring the apparent length of the sunward extent to the dust coma of the comet from the following equation:

$$|v_{ej}| = \frac{\sqrt{2\beta\mu_\odot \Delta \tan \ell \sin \alpha}}{r_H}, \quad (4)$$

in which $\mu_\odot = 3.96 \times 10^{-14} \text{ au}^3 \text{ s}^{-2}$ is the heliocentric gravitational constant, and ℓ is the apparent sunward turn-around angular distance. Our observations show $\ell \approx 2''$ in 2019 September to $\sim 3''$ in 2019 December. By inserting numbers into Equation (4), we find that the ejection speed varied from $|v_{ej}| \approx 5 \text{ m s}^{-1}$ in 2019 September to $\sim 8 \text{ m s}^{-1}$ around perihelion for the optically dominant dust grains with radius $a \sim 0.1 \text{ mm}$. If scaled to dust grains of $\beta \sim 1$, the ejection speed in 2019 September is in good agreement with the result by Guzik et al. (2019, $|v_{ej}| = 44 \pm 14 \text{ m s}^{-1}$).

In order for us to better understand the morphology of the dust tail of 2I, we employ a more realistic Monte Carlo model for cometary ejection of dust to generate synthetic images of comet 2I. Apart from the aforementioned parameters, the brightness profile of the dust coma is also governed by the size distribution of the dust grains, though to a lesser extent. To maintain consistency with activity driven by volatile sublimation, we follow previous literature (e.g., Whipple 1950;

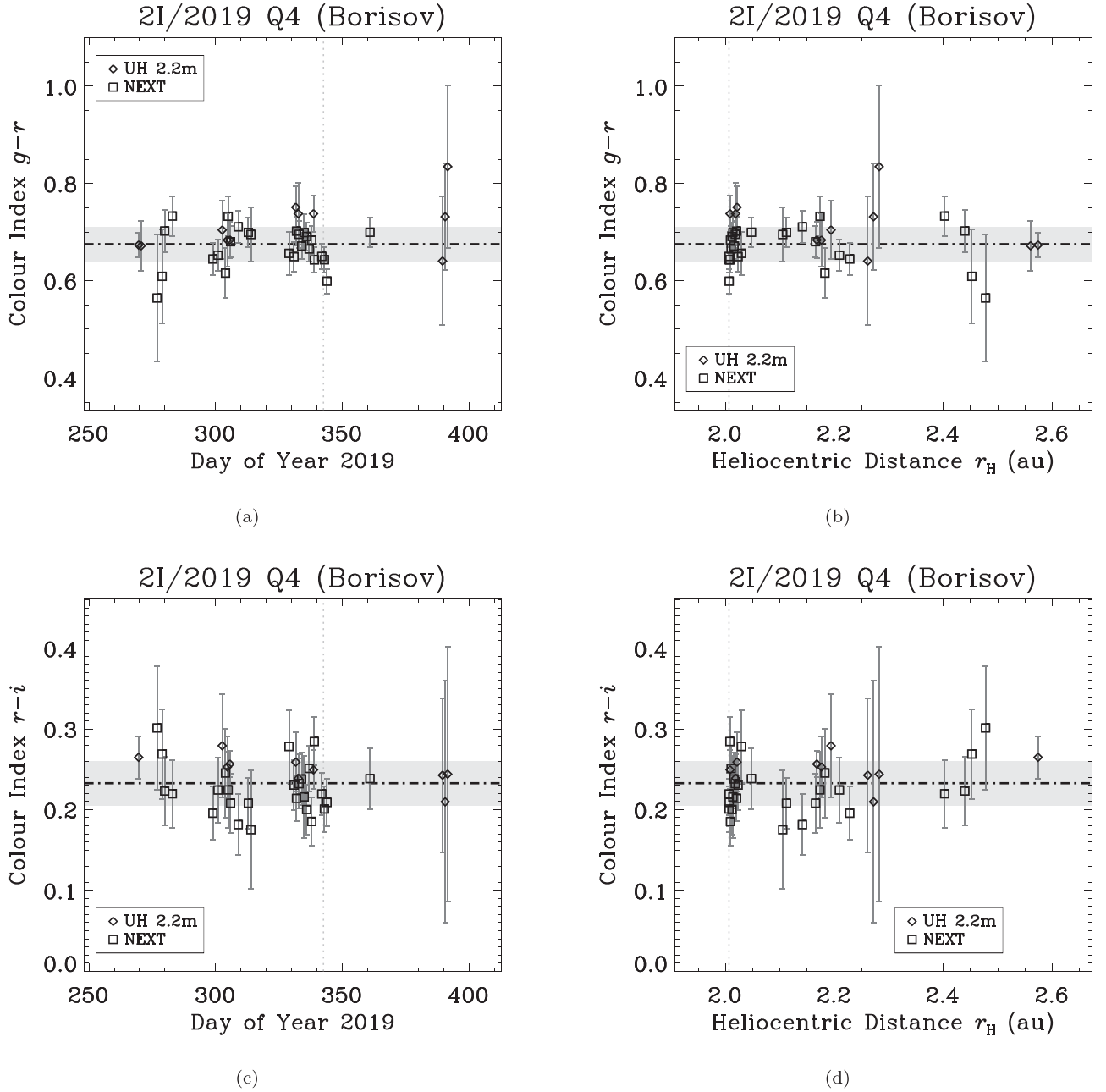


Figure 6. The evolution of the color indices $g - r$ (upper two panels) and $r - i$ (lower two panels) of interstellar comet 2I/2019 Q4 (Borisov) with time (left two panels) and the heliocentric distance (right two panels). Data points from the two observatories are discriminated by different symbols, as indicated in the legends. Taking the measurement uncertainties into consideration, we see no evidence of color variation of the comet. The time-average values of the color indices are represented by a dashed–dotted horizontal line, with the gray zone denoting the $\pm 1\sigma$ uncertainty region, in each of the panels. The perihelion epoch and distance of the comet are marked by vertical gray dotted lines.

Ishiguro 2008) and parameterize the dust ejection speed as

$$|v_{ej}| = V_0 \left(\frac{\beta}{r_H} \right)^{1/2}, \quad (5)$$

where V_0 is the referenced ejection speed for dust grains with $\beta = 1$ ($\sim 1 \mu\text{m}$ in radius) at a heliocentric distance of $r_H = 1 \text{ au}$, and assume a simplistic power-law distribution for the dust size, with a fixed differential power-law index of $\gamma = -3.6$ (Fulle 2004; Guzik et al. 2019). This choice was made because our trial simulation shows that the spatial resolution and the S/N of our images are not sufficient to effectively constrain γ .

In our synthetic models, dust grains are released from the earliest observation of 2I by the ZTF in 2018 December (Ye et al. 2020), following a dust production rate $\sim r_H^{-1}$ to maintain the consistency with the shallowness of the heliocentric distance dependence for the nongravitational effect of the comet (Section 3.2). We use the MERCURY6 package (Chambers 1999) to integrate dust grains with various values of β and the release epochs to the observed epochs, taking gravitational perturbation from the major planets in the solar system into account, although this effect is trivial because the comet has no close encounters with any of the major planets. The Lorentz force is neglected because of its unimportance at

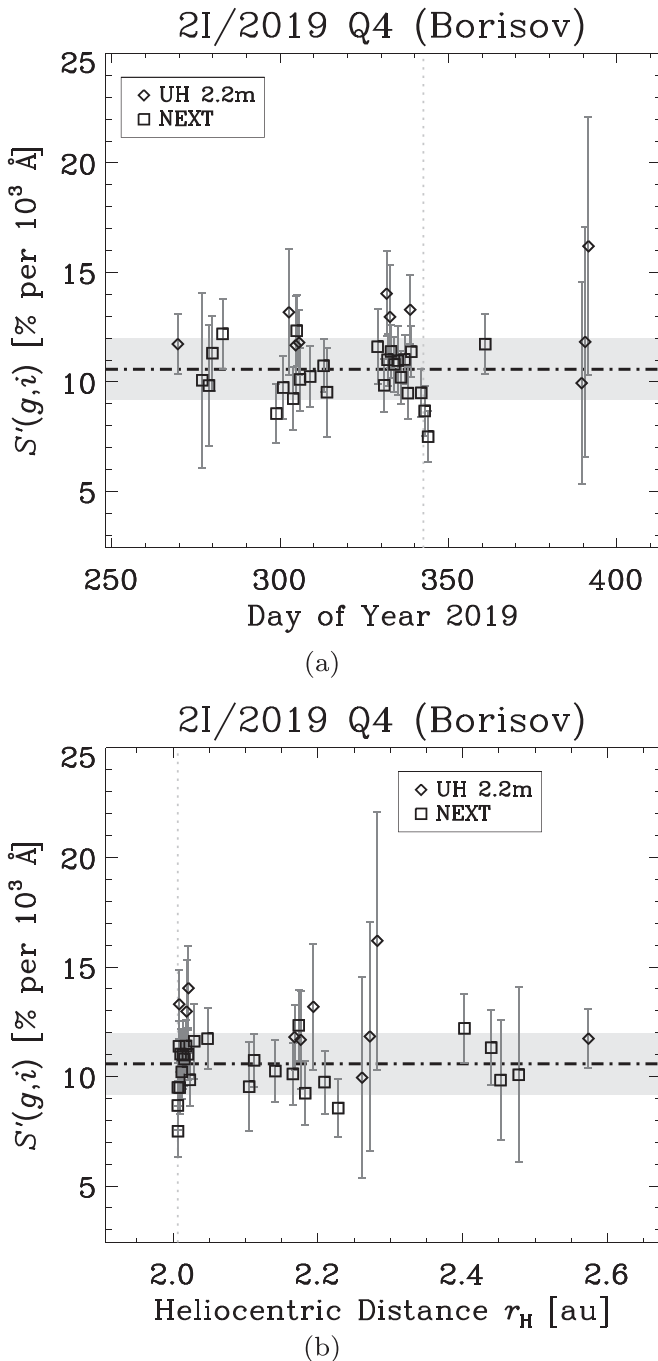


Figure 7. The normalized reflectivity gradient of interstellar comet 2I/2019 Q4 (Borisov) across the g and i bands as a function of time (a) and the heliocentric distance (b). No significant variation is seen. The horizontal dashed-dotted line is the mean value of the normalized reflectivity gradient, with the gray zone representing the associated $\pm 1\sigma$ uncertainty. The vertical gray dotted lines in panels (a) and (b) mark the perihelion epoch and distance of the comet, respectively.

the covered heliocentric distances of 2I (Hui et al. 2019; Jewitt et al. 2019). The tridimensional distribution of the dust grains is then projected onto the sky plane viewed from Earth at some observed epoch. Thereby a bidimensional model image of the comet is formed, which is further convolved with a bidimensional Gaussian function with FWHM equal to the average FWHM of field stars in actual images, so as to mimic observational effects, including the instrumental point-spread effect and atmospheric seeing. The model image is then

Table 3
Best-fit Parameters for Dust Coma Morphology Modeling of Comet 2I/2019 Q4 (Borisov)

Time (UT)	Referenced Ejection Speed V_0 (m s^{-1})	Minimum Radius a_{\min} (m)
2019 Sep 27	70 ± 10	$10^{-4.5 \pm 0.5}$
2019 Oct 29	80 ± 20	$10^{-4.0 \pm 0.5}$
2019 Nov 27	100 ± 20	$10^{-4.0 \pm 1.0}$
2020 Jan 25	140 ± 20	$10^{-5.0 \pm 0.5}$

Note. We test the referenced dust ejection speed V_0 in a step size of 10 m s^{-1} for $V_0 \in [0, 400] \text{ m s}^{-1}$, and the minimum dust radius $a_{\min} \in \{10^{\lfloor \log a_{\min} \rfloor / 2} \cap [10^{-6.5}, 10^{-3.0}]\} \text{ m}$.

compared to the actual observations to identify the ranges of V_0 and a_{\min} that can minimize discrepancies between the two sets of images in the least-squares space. Expectedly and through testing, we cannot constrain the maximum size of the dust grains from our observations, because they do not travel far from the nucleus. We thus somewhat arbitrarily adopt $a_{\max} = 0.1 \text{ m}$ as a fixed parameter.

We summarize the best-fit results in Table 3, with the best-fit models in comparison with observed images shown in Figure 8. Although the assumption of the dust production rate following $\sim r_H^{-1}$ was made to obtain the best-fit results, we found that the results are relatively insensitive to this assumption. For instance, if we instead assume a steeper heliocentric distance dependence for the dust production rate, $\sim r_H^{-2}$, the best-fit results remain completely the same. By applying Equation (5), we can see that the best-fit ejection speed for the optically dominant dust grains in the tail of the comet is in great agreement with the crude estimate from the sunward turnaround point. Our result for the UH 2.2 m observation from 2019 September 27 is consistent with Guzik et al. (2019, $V_0 = 74 \pm 23 \text{ m s}^{-1}$). So is our result for 2019 October, if compared to Kim et al. (2020, $\sim 90 \text{ m s}^{-1}$). Thus, we are confident to conclude that the dust ejection speeds of the comet appear to be low, only $\sim 15\%$ – 30% of the ejection speed given by an ejection model assuming sublimation of water ice. In this regard, 2I is similar to some of the low-activity comets in the solar system, such as 209P/LINEAR (Ye et al. 2016). Meanwhile, we notice that V_0 has possibly been increasing during the period in which we have observed comet. Similar phenomena among solar system comets have been identified observationally (e.g., Tozzi et al. 2011; Moreno et al. 2014). Yet given the large uncertainty we opt not to further interpret it.

Our best-fit results also indicate that the minimum grain size in the distal tail of 2I, which is found to be in a range between $\sim 3 \mu\text{m}$ and 1 mm in radius, is unsurprising in the context of solar system comets (e.g., Fulle 2004). We thereby infer that the activity mechanism on 2I likely resembles that of typical comets in the solar system, whose dust grains are ejected from the surface of the nucleus by coupling with the gas flow of outgassing volatiles.

4.4. Activity

The activity level of the comet can be assessed by investigating its effective geometric scattering cross-section, which we compute from the measurements of r -band magnitude

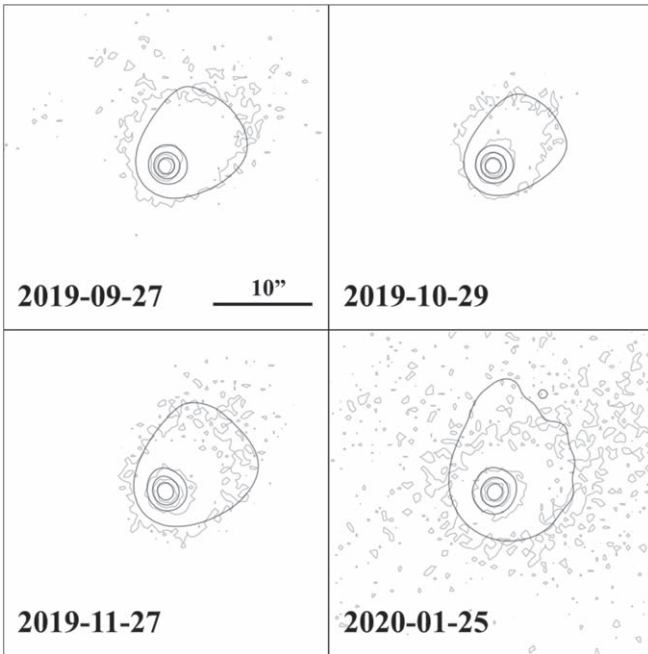


Figure 8. Comparison between the best-fit modeled (white contours) and observed (background images) morphology of interstellar comet 2I/2019 Q4 (Borisov) on selected dates. A scale bar of $10''$ in length, applicable to all of the four panels, is shown. Equatorial north is up and east is left. See Figure 2 for the position angles of the antisolar direction and the negative heliocentric velocity projected onto the sky plane. The best-fit parameters are listed in Table 3.

using the following equation:

$$C_e = \frac{\pi r_0^2}{p_r} 10^{0.4[m_{\odot,r} - m_r(1,1,0)]}, \quad (6)$$

where C_e is the effective scattering cross-section, p_r is the geometric albedo of cometary dust in the coma of the comet, and $m_{\odot,r} = -26.93$ is the apparent r -band magnitude of the Sun at the mean Earth–Sun distance $r_0 = 1.5 \times 10^8$ km (Willmer 2018). So far there is no constraint on the value of p_r of comet 2I, and therefore we assume $p_r = 0.1$ as the appropriate value for cometary dust (e.g., Zubko et al. 2017). The effective cross-section of the comet as a function of time is shown in Figure 9, in which the decline of the intrinsic brightness of the comet is translated to a continuous decline in the effective cross-section within the photometric aperture of $\varrho = 10^4$ km in radius, which can be excellently approximated by a linear function with a best-fit slope of $\overline{C_e} = -0.43 \pm 0.02$ $\text{km}^2 \text{d}^{-1}$. We note that this result is incompatible with the observations by Jewitt & Luu (2019) and Jewitt et al. (2020). However, given the fact that our observation covered a longer period, we argue that there is likely short-term scale variability in the activity of the comet. We do not recall witnessing similar overall trends for the known solar system comets, whose effective scattering cross-sections generally increase and then decrease as they approach and recede from the Sun, respectively, unless outbursts occur. A plausible explanation is that the coma of 2I consists of abundant icy grains that continuously sublimate until exhaustion of volatiles, whereby the effective scattering cross-section diminishes. There exists an alternative explanation that the preperihelion downward

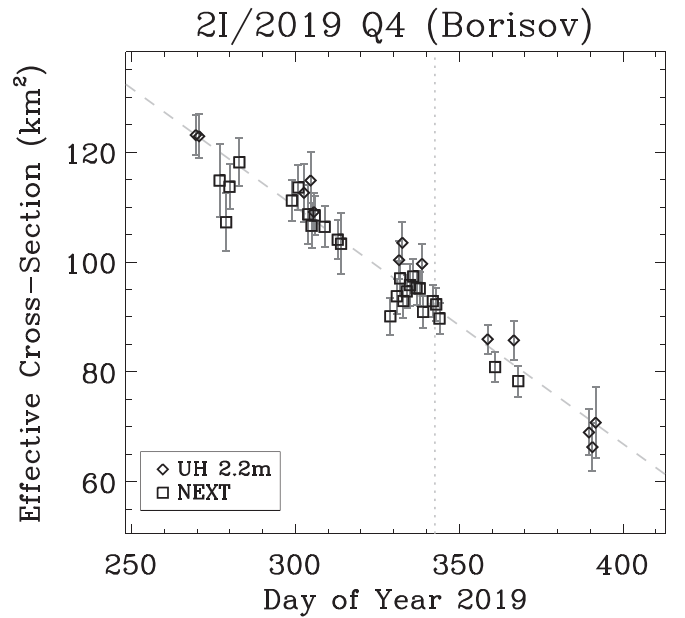


Figure 9. Temporal variation of the effective geometric scattering cross-section, converted from the measurements of r -band magnitude, of interstellar comet 2I/2019 Q4 (Borisov). The downward trend is noticeable. Data points from the two observatories are discriminated by different point symbols as shown in the legend of the plot in the lower left corner. The gray dashed line is the best linear least-squares fit, whereas the vertical dotted gray line marks the perihelion epoch of the comet.

trend in Figure 9 is bogus if the actual phase function of 2I is unprecedentedly steeper than those of the known solar system comets (Section 4.1). Considering the similarities between 2I and solar system comets, we do not prefer this explanation.

The average net mass-loss rate in the fixed-size photometric aperture is related to the mean change rate of the effective cross-section by

$$\overline{\dot{M}_d} = \frac{4}{3} \rho_d \bar{a} \overline{C_e}. \quad (7)$$

Given the difficulty in determining the mean dust radius \bar{a} because the maximum dust size cannot be well constrained, we instead use the optically dominant dust size $\beta \sim 0.01$. Thus we obtain that the average net mass-loss rate of comet 2I is $\overline{\dot{M}_d} \approx -0.4$ kg s^{-1} over the whole observed period. The negative value means that the newly produced mass in the photometric aperture of $\varrho = 10^4$ km fails to supply the mass that leaves the aperture due to the solar radiation pressure and/or nonzero ejection speeds.

As we cannot really constrain the actual mass loss of comet 2I in the above manner, we instead examine it based upon our detection of the nongravitational effect of the comet, in essence owing to the conservation of momentum:

$$\kappa \dot{M}_n v_{\text{out}} = -M_n g(r_H) \sqrt{\sum_{j=1}^3 A_j^2}. \quad (8)$$

Here, $0 \leq \kappa \leq 1$ is the collimation efficiency coefficient of mass ejection, with the lower and upper boundaries corresponding to isotropic and perfectly collimated ejection, respectively, M_n is the mass of the nucleus of the comet, $g(r_H)$ is the adimensional nongravitational force function (tested in Section 3.2 as different power laws $\sim r_H^{-n}$) that follows the

dependence on r_H for the nongravitational acceleration and is normalized at $r_H = 1$ au, and v_{out} is the outflow speed of mass-loss materials, which is approximated by the empirical function given in Combi et al. (2004). As mentioned in Section 3.2, $g(r_H) \sim r_H^{-1 \pm 1}$ is preferred by the fit to the astrometric data of 2I, and therefore we investigate scenarios with three different power-law indices $n = 0, 1, 2$ in the nongravitational force function.

Equation (8) can be separated and integrated to find the expression for the fractional mass erosion of the comet between epochs t_1 and t_2 :

$$\begin{aligned} \mathcal{E}_M(t_1, t_2) &\equiv 1 - \frac{M_n(t_2)}{M_n(t_1)} \\ &\approx \frac{r_0^n}{\kappa} \sqrt{\sum_{j=1}^3 A_j^2} \int_{t_1}^{t_2} \frac{dt}{r_H^n(t) v_{\text{out}}(t)}. \end{aligned} \quad (9)$$

We take $t_1 \approx$ TDB 2018 December 13.5, i.e., the earliest detection of the comet by the ZTF (Ye et al. 2020). The fractional mass erosion of the nucleus as a function of time following the three best-fit nongravitational force models (power-law indices $n = 0, 1,$ and 2) with the assumption of a maximum collimation efficiency coefficient of mass ejection, i.e., $\kappa = 1$, corresponding to perfectly collimated ejection, is plotted in Figure 10. As expected, the nucleus of 2I will be eroded maximally in the case of $n = 0$, because the magnitude of its nongravitational acceleration is a constant, whereas the erosion will be the smallest in the inverse-square case, because the magnitude of the nongravitational acceleration drops the most steeply among the three cases as the heliocentric distance increases. Given the range of the collimation efficiency coefficient, we can conclude that since the earliest detection of the comet by the ZTF in mid-December 2019, $\gtrsim 0.2\%$ of the total nucleus mass has been eroded. The erosion continued to increase as the comet passed perihelion. There is an additional uncertainty in the outflow speed that we have not included in the above calculation, and therefore we suggest that the results for the fractional mass erosion of the comet are better treated as order-of-magnitude estimates.

4.5. Size of the Nucleus

The detection of the nongravitational effect in the motion of 2I enables us to evaluate its nucleus radius. We transform Equation (8) into

$$R_n \approx \left[\frac{3\kappa \mathcal{U} m_H Q v_{\text{out}}}{4\pi \rho_n \sqrt{\sum_{j=1}^3 A_j^2}} \left(\frac{r_H}{r_0} \right)^n \right]^{1/3}, \quad (10)$$

where \mathcal{U} and Q are respectively the molecular weight and the production rate of the dominant mass-loss substance of the comet, and $m_H = 1.66 \times 10^{-27}$ kg is the mass of the hydrogen atom. We assume a typical cometary nucleus density, $\rho_n = 0.5$ g cm $^{-3}$ (e.g., Pätzold et al. 2016). Since 2I is the most CO-rich in the context of solar system comets (Bodewits et al. 2020; Cordiner et al. 2020), with the only exception of C/2016 R2 (PANSTARRS) (McKay et al. 2019), it therefore seems more likely that the detected nongravitational motion of the comet is caused by outflow of CO. We constrain the size of the nucleus using results from Cordiner et al. (2020), who reported

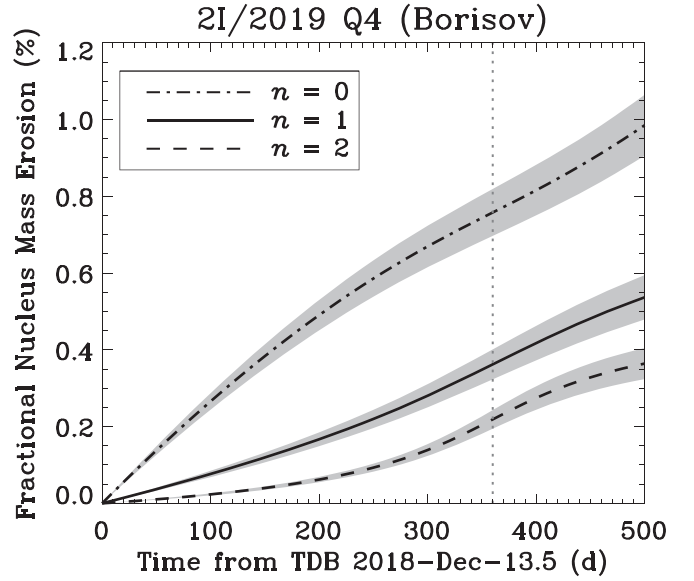


Figure 10. Fractional nucleus mass erosion of interstellar comet 2I/2019 Q4 (Borisov) as a function of time with different power-law indices n in the nongravitational force function (discriminated by line styles, see the legend). The corresponding 1σ uncertainty regions, propagated from the formal errors in the nongravitational parameters, are shaded as gray zones. Here we assume $\kappa = 1$ for the collimation efficiency coefficient, i.e., perfectly collimated mass loss of the nucleus. The vertical dotted gray line is the perihelion epoch of the comet.

$Q_{\text{CO}} = (4.4 \pm 0.7) \times 10^{26}$ s $^{-1}$ at $r_H = 2.01$ au with an outflow speed of $v_{\text{out}} = (4.7 \pm 0.4) \times 10^2$ m s $^{-1}$. Substituting, we find $R_n \lesssim (3.6 \pm 0.3) \times 10^2$ m.

In fact, even if we ignore the fact that the activity of 2I is CO-dominant (Bodewits et al. 2020; Cordiner et al. 2020) but assume momentarily that the nongravitational effect is caused by sublimation of H $_2$ O ice, there is still no major change to the upper limit to the size of the nucleus of 2I. While multiple observers have reported emission lines of the comet (e.g., Fitzsimmons et al. 2019; Opitom et al. 2019; Kareta et al. 2020; McKay et al. 2020), the most straightforward estimate of the mass-loss rate of the comet is constrained from the detection of the forbidden oxygen line ([O I] 6300 Å) by McKay et al. (2020), who assumed that H $_2$ O is the dominant source and derived a production rate of $Q_{\text{H}_2\text{O}} = (6.3 \pm 1.5) \times 10^{26}$ s $^{-1}$ at heliocentric distance $r_H = 2.38$ au. Plugging numbers in, Equation (10) yields an upper limit to the radius of the nucleus of 2I as $R_n \lesssim (3.9 \pm 0.5) \times 10^2$ m, consistent with the estimate using measurements from Cordiner et al. (2020).

We are therefore confident to conclude that, based on our detection of the nongravitational acceleration of 2I, the nucleus is most likely $\lesssim 0.4$ km in radius, in excellent agreement with the Hubble Space Telescope (HST) observation by Jewitt et al. (2020).

5. Summary

We summarize our study of the observations from the UH 2.2 m telescope and 0.6 m NEXT of interstellar comet 2I/2019 Q4 (Borisov) in the following.

1. The intrinsic brightness of the comet was observed to decline starting from late September 2019 to late January 2020, on its way from preperihelion all the way to the outbound leg postperihelion. This behavior, which

appears uncommon in the context of solar system comets without outbursts, is likely explained not by the phase effect but by the downward trend of the effective scattering cross-section due to sublimation of volatiles with a slope of $-0.43 \pm 0.02 \text{ km}^2 \text{ d}^{-1}$.

2. We have a statistically confident detection of the nongravitational acceleration of the comet, which follows a shallow heliocentric distance dependence of $r_H^{-1 \pm 1}$, with the available astrometric observations. By perihelion, a fraction of $\gtrsim 0.2\%$ of the total mass of the nucleus has been eroded since the earliest detection by the ZTF in mid-December 2018.
3. Assuming a typical cometary nucleus density ($\rho_n = 0.5 \text{ g cm}^{-3}$), we estimate from the detected nongravitational effect of the comet that its nucleus is most likely $\lesssim 0.4 \text{ km}$ in radius, in favor of the result from the HST observation by Jewitt et al. (2020).
4. Our morphologic analysis of the dust tail reveals that the ejection speed increased from $\sim 4 \text{ m s}^{-1}$ in 2019 September to $\sim 7 \text{ m s}^{-1}$ for the optically dominant dust grains with $\beta \sim 0.01$ (corresponding to a grain radius of $a \sim 0.1 \text{ mm}$, given an assumed dust bulk density of $\rho_d = 0.5 \text{ g cm}^{-3}$). The dust grains that contribute to the effective geometric scattering cross-section are no smaller than micron size.
5. The color of the comet remained unchanged with the uncertainty taken into consideration, which is, on average, unexceptional in the context of known solar system comets. We determined the mean values of the color as $\langle g - r \rangle = 0.68 \pm 0.04$, $\langle r - i \rangle = 0.23 \pm 0.03$, and the normalized reflectivity gradient over the g and i bands $\overline{r}(g, i) = (10.6 \pm 1.4)\%$ per 10^3 \AA .

We thank Luke McKay and the engineer team of the UH 2.2 m telescope, as well as Xing Gao of Xingming Observatory, for technical assistance. We also thank Davide Farnocchia, Bill Gray, David Jewitt, Yoonyoung Kim, and Adam McKay for insightful help and discussions, and the observers who submitted good-quality astrometric measurements of the comet to the MPC. Comments from an anonymous reviewer greatly help us improve the quality of this work. The research was funded by NASA Near Earth Object Observations grant No. NNX13AI64G to D.J.T.

Software: FindOrb, HOTPANTS (Becker 2015), IDL, IRAF, L.A.Cosmic (van Dokkum 2001), MERCURY6 (Chambers 1999), StarFinder (Diolaiti et al. 2000).

ORCID iDs

Man-To Hui (許文韜) <https://orcid.org/0000-0001-9067-7477>
 Quan-Zhi Ye (葉泉志) <https://orcid.org/0000-0002-4838-7676>
 David J. Tholen <https://orcid.org/0000-0003-0773-1888>

References

A'Hearn, M. F., Schleicher, D. G., Millis, R. L., Feldman, P. D., & Thompson, D. T. 1984, *AJ*, 89, 579
 Bannister, M. T., Opitom, C., Fitzsimmons, A., et al. 2020, arXiv:2001.11605

Bannister, M. T., Schwamb, M. E., Fraser, W. C., et al. 2017, *ApJL*, 851, L38
 Becker, A. 2015, HOTPANTS: High Order Transform of PSF ANd Template Subtraction, ascl:1504.004
 Bertini, I., la Forgia, F., Fulle, M., et al. 2019, *MNRAS*, 482, 2924
 Bodewits, D., Noonan, J. W., Feldman, P. D., et al. 2020, *NatAs*, in press
 Bolin, B. T., Lisse, C. M., Kasliwal, M. M., et al. 2020, *AJ*, 160, 26
 Chambers, J. E. 1999, *MNRAS*, 304, 793
 Combi, M., Shou, Y., Fougere, N., et al. 2020, *Icar*, 335, 113421
 Combi, M. R., Harris, W. M., & Smyth, W. H. 2004, in *Comets II*, ed. M. C. Festou, H. U. Keller, & H. A. Weaver (Tucson, AZ: Univ. Arizona Press), 523
 Cordiner, M. A., Milam, S. N., Biver, N., et al. 2020, *NatAs*, in press
 de León, J., Licandro, J., Serra-Ricart, M., et al. 2019, *RNAAS*, 3, 131
 Diolaiti, E., Bendinelli, O., Bonaccini, D., et al. 2000, *A&AS*, 147, 335
 Dybczyński, P. A., & Królikowska, M. 2018, *A&A*, 610, L11
 Farnocchia, D., Chesley, S. R., Chamberlin, A. B., & Tholen, D. J. 2015, *Icar*, 245, 94
 Fink, U., & Doose, L. 2018, *Icar*, 309, 265
 Finson, M. J., & Probstein, R. F. 1968, *ApJ*, 154, 327
 Fitzsimmons, A., Hainaut, O., Meech, K. J., et al. 2019, *ApJL*, 885, L9
 Flewelling, H. A., Magnier, E. A., Chambers, K. C., et al. 2016, arXiv:1612.05243
 Folkner, W. M., Williams, J. G., Boggs, D. H., Park, R. S., & Kuchynka, P. 2014, *IPNPR*, 196, 1
 Fougere, N., Altwegg, K., Berthelier, J.-J., et al. 2016, *MNRAS*, 462, S156
 Fulle, M. 2004, in *Comets II*, ed. M. C. Festou, H. U. Keller, & H. A. Weaver (Tucson, AZ: Univ. Arizona Press), 565
 Gaia Collaboration, Brown, A. G. A., Vallenari, A., et al. 2018, *A&A*, 616, A1
 Guzik, P., Drahus, M., Rusek, K., et al. 2019, *NatAs*, 4, 53
 Henden, A. A., Levine, S., Terrell, D., et al. 2018, *AAS Meeting Abstracts*, 232, 223.06
 Higuchi, A., & Kokubo, E. 2019, *MNRAS*, 492, 268
 Hui, M.-T., Farnocchia, D., & Micheli, M. 2019, *AJ*, 157, 162
 Hui, M.-T., & Jewitt, D. 2017, *AJ*, 153, 80
 Ishiguro, M. 2008, *Icar*, 193, 96
 Jewitt, D. 1991, in *IAU Coll. 116, Comets in the Post-Halley Era*, 167, ed. R. L. Newburn, Jr., M. Neugebauer, & J. Rahe (Dordrecht: Kluwer), 19
 Jewitt, D., Hui, M.-T., Kim, Y., et al. 2020, *ApJL*, 888, L23
 Jewitt, D., Kim, Y., Luu, J., et al. 2019, *AJ*, 157, 103
 Jewitt, D., & Luu, J. 2019, *ApJL*, 886, L29
 Jewitt, D., Luu, J., Rajagopal, J., et al. 2017, *ApJL*, 850, L36
 Jewitt, D., & Meech, K. J. 1986, *ApJ*, 310, 937
 Jordi, K., Grebel, E. K., & Ammon, K. 2006, *A&A*, 460, 339
 Karetta, T., Andrews, J., Noonan, J. W., et al. 2020, *ApJL*, 889, L38
 Kim, Y., Jewitt, D., Mutchler, M., et al. 2020, *ApJL*, 895, L34
 Knight, M. M., Protopapa, S., Kelley, M. S. P., et al. 2017, *ApJL*, 851, L31
 Licandro, J., Popescu, M., de León, J., et al. 2018, *A&A*, 618, A170
 Marcus, J. N. 2007, *ICQ*, 29, 39
 Marsden, B. G., Sekanina, Z., & Yeomans, D. K. 1973, *AJ*, 78, 211
 McKay, A. J., Cochran, A. L., Dello Russo, N., et al. 2020, *ApJL*, 889, L10
 McKay, A. J., DiSanti, M. A., Kelley, M. S. P., et al. 2019, *AJ*, 158, 128
 Meech, K. J., & Jewitt, D. C. 1987, *A&A*, 187, 585
 Moreno, F., Pozuelos, F., Aceituno, F., et al. 2014, *ApJ*, 791, 118
 Opitom, C., Fitzsimmons, A., Jehin, E., et al. 2019, *A&A*, 631, L8
 Pätzold, M., Andert, T., Hahn, M., et al. 2016, *Natur*, 530, 63
 Schleicher, D. G., & Bair, A. N. 2011, *AJ*, 141, 177
 Tonry, J. L., Stubbs, C. W., Lykke, K. R., et al. 2012, *ApJ*, 750, 99
 Tozzi, G. P., Patriarchi, P., Boehnhardt, H., et al. 2011, *A&A*, 531, A54
 van Dokkum, P. G. 2001, *PASP*, 113, 1420
 Vereš, P., Farnocchia, D., Chesley, S. R., & Chamberlin, A. B. 2017, *Icar*, 296, 139
 Whipple, F. L. 1950, *ApJ*, 111, 375
 Willmer, C. N. A. 2018, *ApJS*, 236, 47
 Ye, Q., Kelley, M. S. P., Bolin, B. T., et al. 2020, *AJ*, 159, 77
 Ye, Q.-Z., Hui, M.-T., Brown, P. G., et al. 2016, *Icar*, 264, 48
 Zubko, E., Videen, G., Shkuratov, Y., et al. 2017, *QJST*, 202, 104